nature communications

Article

https://doi.org/10.1038/s41467-025-65585-3

Controlling rotational air lasing lineshape by carrier-envelope offset phase

Received: 3 May 2025

Accepted: 15 October 2025

Published online: 31 October 2025

Check for updates

Jingsong Gao[1], Hao Liang[2] ✉, Mahmudul Hasan[1], Chi-Hong Yuen[3], Ming-Shian Tsai[4], Ming-Chang Chen[4], Chii-Dong Lin[1], Kiyoshi Ueda[5,6], Hans Jakob Wörner[7] & Meng Han[1] ✉

The carrier-envelope offset phase (CEP) of a few-cycle optical pulse is commonly used to control electron dynamics on the attosecond timescale, whereas lasing spectra from transitions between rotational states are generally emitted over much longer durations, typically nanoseconds. Here, we demonstrate CEP control of the rotational lasing spectra corresponding to the transition from $B^2\Sigma_u^+(0)$ to $X^2\Sigma_g^+(1)$ in N_2^+ cations, transforming its lineshape from a symmetric Lorentzian profile to an asymmetric Fano type–and vice versa. This lineshape modulation arises from the interference between the B-X coherence initiated by the main pulse and the supercontinuum (self seed) by self-phase modulation, resembling an "f-to-3f" interferometry. Additionally, for lasing lines with lower rotational quantum numbers, we observe a stronger coupling between adjacent lasing peaks, which originates from the amplification of both even- and odd-order rotational coherent emission lines. Our study presents a general framework for controlling lasing lineshapes and provides new insights into sub-optical-cycle dynamics in air lasing.

Spectroscopy is an essential tool for uncovering molecular structures and dynamics in light-matter interactions. The observed spectral line positions reveal energy separations of the transition states, whereas the lineshapes are determined by how matter relaxes after light is resonantly absorbed. For example, when a discrete state is resonantly excited by a light field, the corresponding emission or absorption spectrum will show a symmetric Lorentz lineshape. If the discrete state is coupled with a continuum, the pathway interference between them will result in an asymmetric Fano lineshape, such as the double excited states in helium atoms[1–3]. Pioneering works by Ott et al.[4] demonstrate that the absorption spectral lineshape can be switched between Lorentz and Fano types by the Stark shift induced phase, which depends on the light intensity of the used laser field[5].

Recently, N_2^+ air lasing–a remarkable form of remote, mirrorless optical amplification using air constituent N_2 molecules as the gain medium–has garnered significant attention[6] since its discovery by Yao et al.[7] in 2011. It was observed that the dominant radiations from N_2^+ are around 391 nm and 428 nm, corresponding to the transition from $B^2\Sigma_u^+(\nu'=0)$ to $X^2\Sigma_g^+(\nu=0)$ and from $B^2\Sigma_u^+(\nu'=0)$ to $X^2\Sigma_g^+(\nu=1)$, respectively. The number in the parentheses denotes the vibrational quantum number. The potential population inversion between the B and X states, which contrasts with well-established strong-field theory[8], can be explained by the ionization and post-coupling model[9–13] without accounting for molecular rotational dynamics. In contrast, a rotation-state-resolved experiment[14] and several theoretical studies[15,16] suggest that a significant disparity in rotational distributions between the upper and lower emission levels could, in principle, lead to gain without net electronic population inversion. Other experimental studies[17–24] further highlight the complexity of rotational air lasing. Thus, the underlying mechanism of air lasing remains unclear at the level of rotational states. Notably, although most previous studies have focused on the intensity of air lasing, several recent

[1]J. R. Macdonald Laboratory, Kansas State University, Manhattan, KS, USA. [2]Max Planck Institute for the Physics of Complex Systems, Dresden, Germany. [3]Department of Physics, Kennesaw State University, Marietta, GA, USA. [4]Institute of Photonics Technologies, National Tsing Hua University, Hsinchu, Taiwan. [5]Department of Chemistry, Tohoku University, Sendai, Japan. [6]School of Physical Science and Technology, ShanghaiTech University, Shanghai, China. [7]Laboratory of Physical Chemistry, ETH Zürich, Zürich, Switzerland. ✉e-mail: liangh@pks.mpg.de; meng9@ksu.edu

experiments[11,25,26] have shown that its lineshape is nontrivial and can be controlled with the assistance of Stark effect[25]. Although few-cycle short pulses were applied into air lasing[9,27], the CEP of the driving laser pulses was not stabilized, preventing the revelation of sub-cycle electron dynamics, which has been extensively discussed in theoretical simulations[11,12,28,29]. For example, supercontinuum generation by self-phase modulation (SPM), which is delayed in time with respect to the "red" main pulse due to smaller group velocity at higher frequency in normal dispersion materials, is a typical process when using few-cycle short pulses. The previous study[9] showed the supercontinuum can act as a seed in the intensity amplification of air lasing. However, the coherence and interference between the supercontinuum and the molecular ionic polarization created by the main pulse remain unclear.

In this work, we report the first air lasing experiment with CEP control. We demonstrate the lineshape of the rotation-state-resolved air lasing spectra can be continuously controlled from Lorentz to Fano types and vice versa. The lineshape control is attributed to the interference between the Lorentz-shape free-induction decay (FID) emission governed by the B-X coherence initiated by the main pulse and the self-seed supercontinuum generated by SPM. The two interfering spectral components have different CEP periodicities in their phases, resembling a 'f-to-3f' interferometer. In this experiment, the CEP of the driving pulse is intricately linked to the Fano phase factor in the time-domain representation. By fitting the experimental results using the Fano formalism, we show that FID emission lines with lower rotational quantum numbers undergo amplification, leading to lasing action. By comparing the CEP dependence between low- and high-order rotational lasing lines, our study reveals that electronic population inversion is not the sole factor determining lasing action; molecular rotational dynamics also play a crucial role.

Results

The laser system used in this experiment is a CEP-stabilized sub-4 femtosecond Yb laser with a spectrum covering both visible and near-infrared (IR) from 580 nm to 1300 nm, characterized by both transient-grating FROG (frequency-resolved optical gating) and TIPTOE (tunneling ionization with a perturbation for the time-domain observation of an electric field) measurements. The CEP stabilization is actively maintained through both fast and slow feedback loops, ensuring a stability of better than 200 mrad standard deviation over 14 h. For further laser details, refer to refs. 30–32. To optimize pulse dispersion and vary the CEP value, we adjusted the thickness of a fused-silica wedge pair (3.5 degrees) inserted into the beam path using a piezoelectric delay stage. The relative CEP value is calibrated by the difference between the group velocity and the phase velocity in fused silica at the center wavelength of 900 nm. In our experiments, we used ~200 μJ for single pulse energy. The pulse was focused by a silver concave mirror with a focal length of 35 cm, achieving an estimated peak intensity of 2×10^{14} W/cm^2. Short-pass ultraviolet (UV) filters with a cutoff of 450 nm were employed to block the visible driving beam. Two spectrometers were used to measure the air lasing spectrum: one with a broader measurement range (200–1100 nm) but lower resolution (~0.2 nm), and the other with higher resolution (~0.01 nm) but a limited measurement range (424–429 nm). We present more experimental details in Supplementary Information (SI).

In Fig. 1a, we show a photograph of our gas tube filled with pure N_2, taken during the generation of air lasing. The strong electric field of the light pulse can easily tunnel-ionize several valence orbitals of the N_2 molecules, producing a bright plasma filament. As illustrated in the image, the plasma filament emits a white light beam when the driving light pulse is optimized to an ultrashort, near-single-cycle timescale. During this filamentation, nitrogen molecules are primarily ionized into the three lowest electronic states of N_2^+, with lasing emissions occurring from the transition between the second excited state ($B^2\Sigma_u^+$) and the ground state ($X^2\Sigma_g^+$). Figure 1b presents a comparison of the air lasing spectra at high and low gas pressures, specifically 1 bar and 1 mbar. The sharp lasing peaks around 391 nm and 428 nm correspond to transitions between different vibrational states, with the 391 nm peak associated with $\nu' = 0 \rightarrow \nu = 0$ and the 428 nm peak corresponding to $\nu' = 0 \rightarrow \nu = 1$, where ν' and ν represent the vibrational quantum numbers of the upper and lower states, respectively. Another mechanism that generates new frequencies is SPM, which is a third-order nonlinearity-based parametric process. SPM generally occurs under high gas pressure and it is delayed in time compared to the main IR pulse. As shown in Fig. 1b, the pronounced pedestal in the blue curve represents the white light generated by SPM under atmospheric pressure. When the gas pressure is reduced to 1 mbar, the white light nearly disappears, as shown by the orange curve.

Supplementary Information Fig. 1 presents additional experimental evidence supporting the lasing nature of the forward-emitted light. We first measured the beam profile after the emission propagated 5 m through air and observed that the air lasing beam exhibits a significantly smaller divergence angle of less than 10 mrad compared to the pump beam. Furthermore, polarization-resolved measurements confirm that the air lasing is linearly polarized–consistent with the polarization of the pump pulse–while the side-emitted air fluorescence is approximately unpolarized.

In Fig. 1c, we present the high-resolution spectrum around 428 nm at 1 mbar, which resolves transitions between rotational states, specifically the R and P branches. The R and P branches correspond to rotational transitions of $(J' + 1 \rightarrow J)$ and $(J' - 1 \rightarrow J)$, respectively, where J' and J denote the rotational quantum numbers of the upper and lower states. In Fig. 1c, the numbers associated with the peaks, indicated by dashed lines, represent the rotational quantum number J of the $X^2\Sigma_g^+(\nu = 1)$ state. In our experiment, the spectral lines in the P branch could not be resolved with the spectrometers used. Therefore, this study focuses on analyzing the lineshape variations of the R branch of the 428-nm lasing.

Figure 1c demonstrates that SPM influences both the lineshapes and peak positions of rotational-state-resolved air lasing spectra. At 1 mbar, where SPM is absent, the R-branch lasing peaks exhibit a symmetrical Lorentzian profile, a characteristic feature of FID emission, allowing for accurate peak assignment (see the dashed lines and labeled numbers). The even-order lasing peaks are stronger than the odd-order transitions due to nuclear spin multiplicity. In contrast, at 1 bar, where SPM is strong, both the peak positions and lineshapes undergo slight modifications, indicating a coherent superposition of SPM and FID emission.

We further investigate the CEP dependence of N_2^+ lasing spectra. In the Supplementary Information Fig. 2, we show the measured CEP-resolved lasing spectra at different gas pressures with the broad-range spectrometer. At a pressure of 1 mbar, no significant CEP dependence is observed. However, as the gas pressure increases to several hundred torr, the lasing spectra exhibit a strong dependence on the laser CEP. Figure 2a presents the measured CEP dependence of the R-branch 428-nm lasing with the high-resolution spectrometer at 1 bar. Each spectral line shows a clear CEP dependence with a periodicity of π, corresponding a oscillation of $\cos(2\Phi_{CEP})$. This dependence cannot be solely attributed to SPM, as the SPM field, $E_{SPM}(\omega)$, originates from the third-order-nonlinear polarization (i.e., degenerate four-wave mixing) of the incident field, $E_0(\omega)e^{i\Phi_{CEP}}$. The SPM is expressed as $E_{SPM}(\omega_1 - \omega_2 + \omega_3) \propto E_0(\omega_1)E_0^*(\omega_2)E_0(\omega_3)e^{i\Phi_{CEP}}$, which introduces a CEP dependence only in the phase factor, mirroring the CEP of the incident driving field[33]. Since the spectral intensity of SPM does not depend on the laser CEP, a more natural explanation involves the interference between SPM and the B-X coherence created by the main pulse, where the terms have different CEP dependence in their phases. This interference is analogous to the spectral beating observed between the fundamental field and its second harmonic in f-to-2f CEP interferometry[34–38]. The measured π periodicity in Fig. 2a suggests that

the phase of B-X coherence must be governed by $e^{i3\Phi_{CEP}}$, leading us to refer to this spectral beating as "f-to-3f" interferometry. The energy separation between the B and X states corresponds to approximately three photons of the driving laser field with the assistance of dynamic AC Stark shift[11,39], resulting in the CEP-dependent phase factor $e^{i3\Phi_{CEP}}$. In SI, we present the calculated phase evolution of FID governed by B-X coherence driven by the main IR pulse as a function of CEP using a density matrix approach for strong-field ionization[12,13,40]. The calculations align well with the observed phase factor $e^{i3\Phi_{CEP}}$. After the generation of the B-X coherence, the seed injection and interference processes are not sequential. In fact, the seeding process can be understood as an interferometric process. In SI, we discuss the seeding process based on a two-level optical Bloch equation.

Beyond the observed π periodicity, the evolution of the lineshape within a single period is particularly intriguing. Figure 2b presents two lineouts in the $J = 14$ lasing regime at CEP values of 0 and 0.25π. The lineshape transitions from a symmetric Lorentzian profile at CEP = 0 to an asymmetric Fano profile at CEP = 0.25π. Notably, the peak position shifts along the dashed red curve in Fig. 2a. Figure 2c displays the corresponding lineouts in the $J = 7, 8$ regime. At CEP = 0, the $J = 7$ peak is largely suppressed, while the $J = 8$ peak retains a symmetric Lorentzian shape. However, at CEP = 0.25π, both peaks emerge with an asymmetric Fano profile. A comparison between low- and high-rotational quantum number regimes reveals a distinct trend: in the laser field the weak odd-order lasing lines with lower J values (e.g., $J = 5, 7, 9$) are significantly enhanced, whereas those with higher J values (e.g., $J = 13, 15$) remain considerably weaker. Supplementary Information Fig. 3 presents the full range of the CEP-resolved air lasing spectrum, including the P branch and the region around the 391-nm line. We verified that the lineshapes of both exhibit a similar CEP dependence as the R branch at 428 nm shown here.

Figure 3 illustrates the formation mechanism of the Fano lineshape, arising from the interference between SPM and FID emission. Since we focus on a narrow wavelength range of a few nanometers around 428 nm corresponding to a picosecond timescale, the SPM field, which retains a femtosecond-scale temporal profile similar to the incident field, can be approximated as a delta function in the time domain. Taking the arrival time of the laser pulse as time zero, the SPM field remains constant in both phase and amplitude in the frequency domain. Simultaneously, the B-X coherence of the rotational states is excited at time zero and decays via FID emission with a time-dependent profile of $\exp(-i\omega_0 t - \Gamma t/2)\Theta(t)$, where ω_0 is the energy separation between the upper and bottom states, Γ is related to the lifetime of the upper state and $\Theta(t)$ is Heaviside step function. The corresponding frequency-domain representation of FID emission follows a Lorentzian distribution, given by $i/(\omega - \omega_0 + i\Gamma/2)$, with

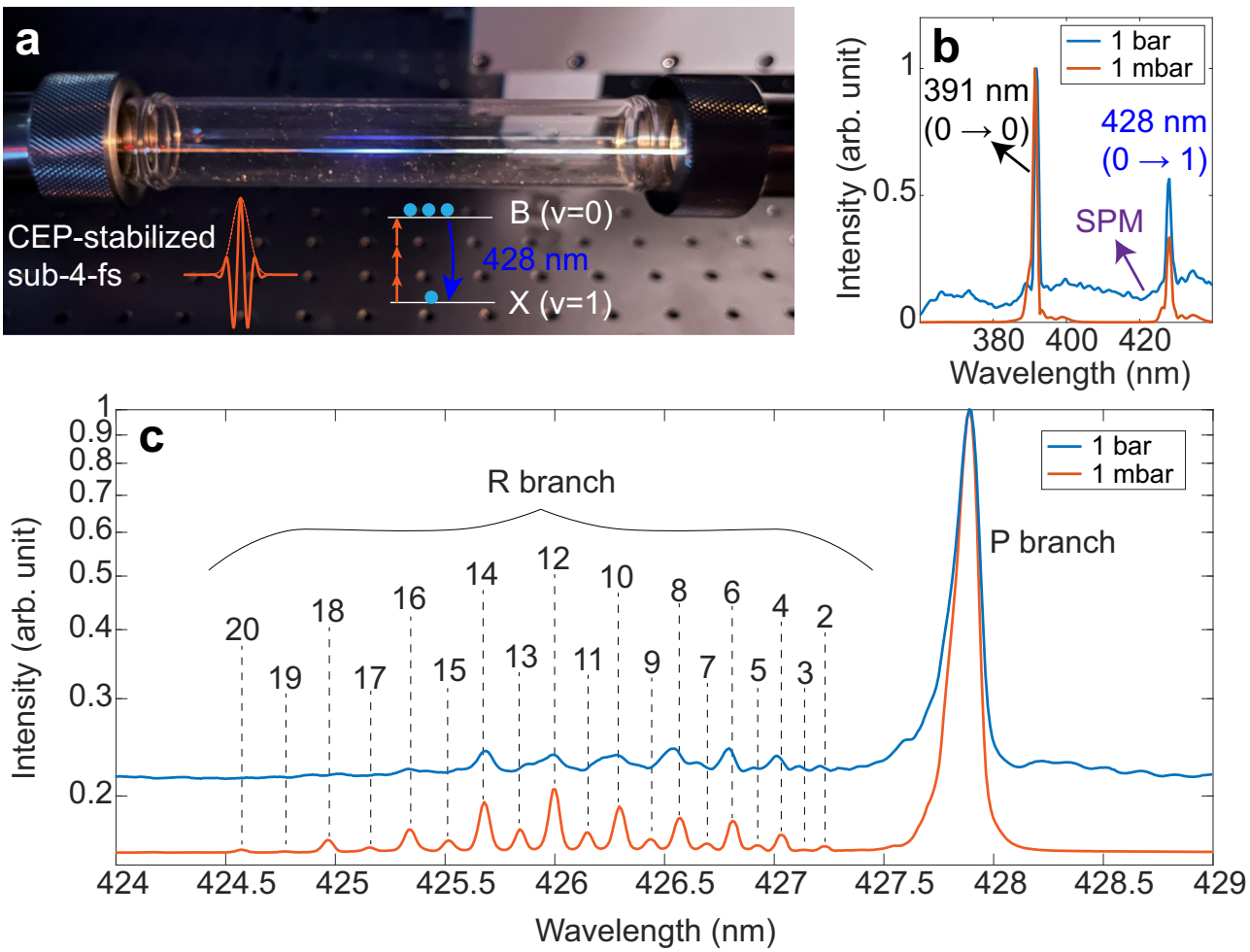

Fig. 1 | Air lasing generation by CEP-stabilized near-single-cycle light pulses. **a** Photo of a gas tube filled with 1 bar N_2, where the laser beam is propagating from left to right and focused in the tube center. **b** Measured lasing spectra after a short-pass UV filter (<450 nm) at the gas pressure of 1 bar and 1 mbar, respectively. In the 1 bar case, the pedestal is corresponding to the supercontinuum labeled with SPM. **c** High-energy-resolution lasing spectra around 428 nm, where the rotational quantum number of the $X^2\Sigma_g^+(v=1)$ state is assigned on the top of the peaks in the spectrum at 1 mbar. In the high-pressure case, the peak positions and lineshapes are both varied and dependent on the laser CEP.

https://doi.org/10.1038/s41467-025-65585-3

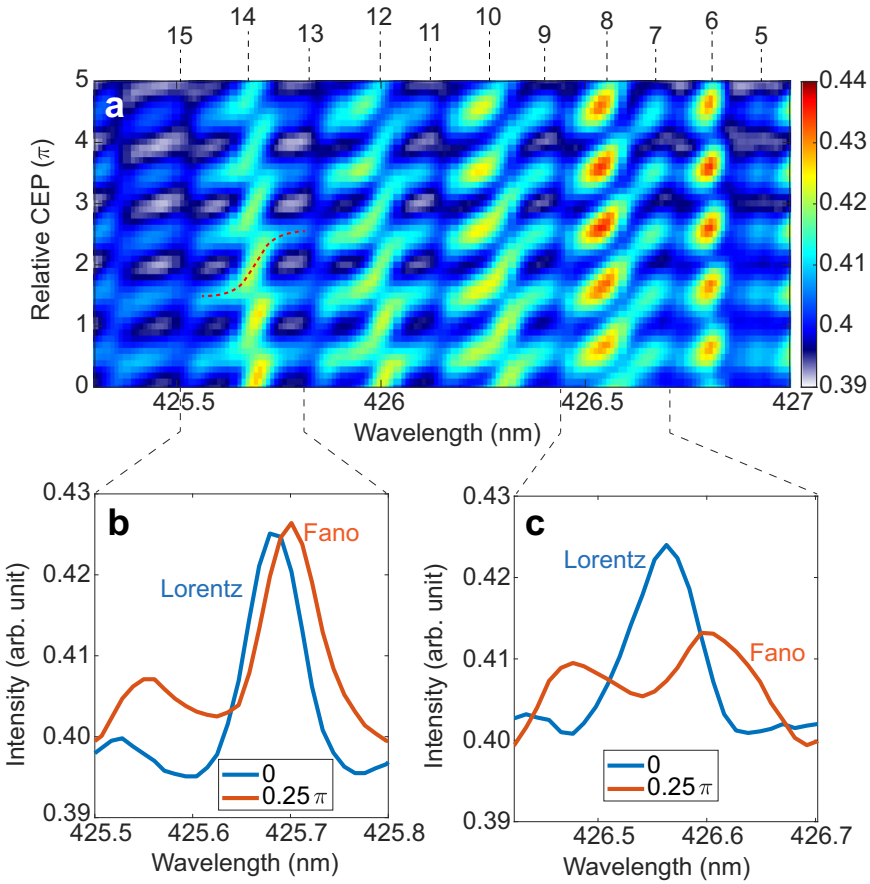

Fig. 2 | Controlling rotational lasing lineshape with CEP. a Measured CEP-resolved R branch of the 428-nm N_2^+ lasing spectrum. The slight non-periodicity along the CEP axis is attributed to the chirp effect induced by variations in the inserted thickness of the fused-silica wedge pair. **b**, **c** Several lineouts from (**a**) to highlight the lineshape change at different CEPs.

$1/\sqrt{(\omega-\omega_0)^2+(\Gamma/2)^2}$ for its amplitude square and arc tangent function $\arctan[2(\omega-\omega_0)/\Gamma]$ for its phase, as depicted by the blue and green curves in Fig. 3a, respectively. The superposition of a constant background and a Lorentzian distribution always results in a Fano lineshape[41], up to an overall shift.

By varying the CEP of the incident field, one can control the phase difference between SPM and FID emission, given by $\Delta\Phi = 2\Phi_{CEP}$, which is equivalent to shifting the SPM phase (magenta line in Fig. 3a) vertically in the plot. Consequently, the CEP precisely determines the position of constructive interference in the energy domain and thus the peak position of the resulting lineshape. For $\Delta\Phi \in (0, \pi)$, the intersection between the magenta and green curves is in the right side of ω_0, leading to a peak shifted to the right–corresponding to a Fano lineshape with a Fano parameter of $q < 0$. Conversely, for $\Delta\Phi \in (-\pi, 0)$, the peak is on the left side, corresponding to $q > 0$. At the positions of $\Delta\Phi = 0$ and $\pm\pi$, the lineshape reduces to a symmetric Lorentzian profile, corresponding to $q = 0$ or ∞. In Fig. 3b, we illustrate the lineshapes resulting from the superposition of SPM and FID emission for CEP values of 0 and 0.25 π, which reproduce the Lorentzian and Fano profiles, respectively. It is important to note that spectral congestion–where adjacent lasing lines are too closely spaced (specially for the low-J lines)–may cause the experimentally observed asymmetry to be less pronounced compared to the theoretical model. In high pressures, the THG might start to play a role, specially at short wavelengths such as 391 nm. An improved model should account for THG as well.

Figure 3c–e depicts the physical picture of the interference in the time domain. The CEP determines the azimuthal angle of the two functions in the complex plane at time zero. This initial phase controls the projection of the Lorentz dipole function onto the direction of the delta function. The projection components along the same direction can interfere with each other. In Fig. 3e, we illustrate the projects of dipole $d(t)$ along the direction of SPM at CEP of 0 and 0.25 π, respectively. At CEP = 0, the dipole starts from its maximum value before oscillating and gradually decaying. In contrast, at CEP = 0.25 π, where the Lorentz dipole function is perpendicular to the delta function, the dipole projection starts from zero. The phase offset in the time domain is referred to as the Fano phase Φ_{Fano}, which is uniquely related to the Fano parameter q[4]. In the pioneering work[4], the Fano phase was identified as the AC-Stark-induced phase shift in a strong IR field. In our case, however, the Fano phase corresponds precisely to the phase difference between the two interfering channels, given by $2\Phi_{CEP}$.

Above analysis is based on the approximation that the SPM won't be amplified in the lasing process. Now we discuss more details about light amplification. We fit the experiment data Fig. 2a using $P(\Phi_{CEP};\lambda) = |u(\lambda)e^{i\Phi_{CEP}} + v(\lambda)e^{3i\Phi_{CEP}}|^2 = a(\lambda) + b(\lambda)\cos[2\Phi_{CEP} - \phi_0(\lambda)]$ for each wavelength λ, describing the interference between SPM $u(\lambda)$ and FID emission $v(\lambda)$. The fitting result is shown in Fig. 4a, which agrees well with the experiment data. Here $\phi_0 = \arg[uv^*]$ represents the phase difference between them, $a = |u|^2 + |v|^2$ and $b = 2|uv|$ gives the background and the amplitude of the oscillation, respectively. The fit indicates that the intensity of FID emission is two orders of magnitude lower than that of the SPM, leading to $a \approx |u|^2$, as shown in Fig. 4b. The distribution of a suggests that SPM acts as a seed for lasing, with

https://doi.org/10.1038/s41467-025-65585-3

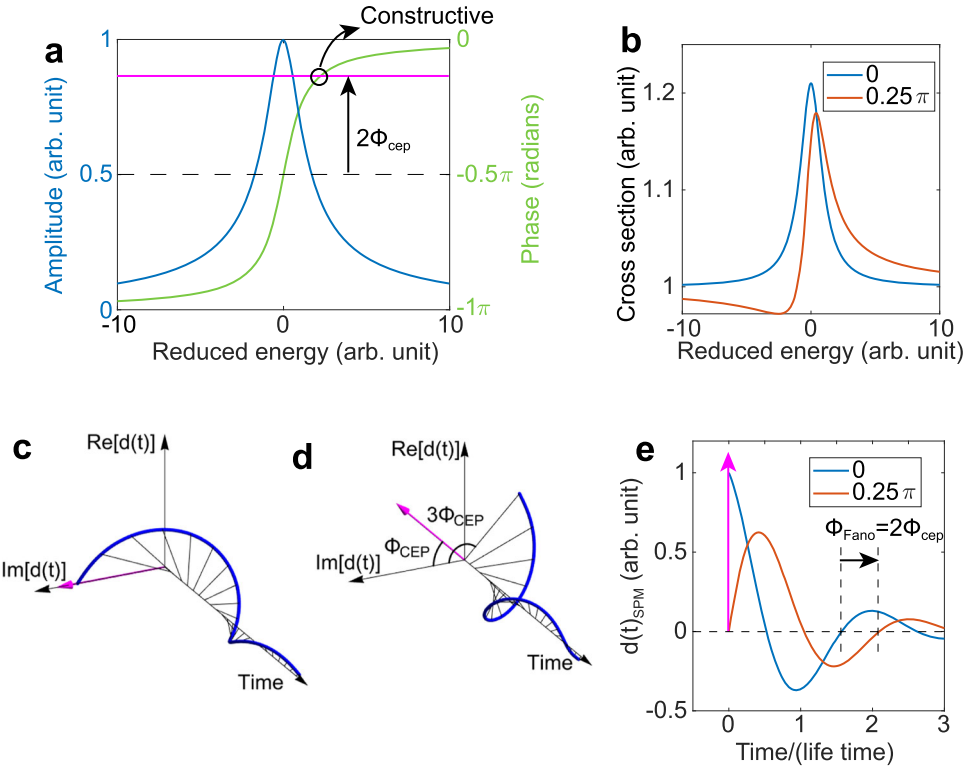

Fig. 3 | Mechanism of lineshape control. a Amplitude (blue solid line) and phase (green solid line) distribution of a Lorentz lineshape corresponding to one rotational lasing line. The phase of SPM is approximately flat and represented with the magenta line, whereas the SPM amplitude is a constant number (not shown). The relative phase difference between the SPM and the central position (i.e. resonant energy) of the lasing line is $2\Phi_{CEP}$. The intersection between the green curve and the magenta line is corresponding to the relative phase difference of zero, giving rise to a constructive interference. **b** Calculated lineshapes after the interference between SPM and Lorentz lineshape at the CEP of 0 and 0.25π. Time-domain pictures for the interference between SPM and Lorentz dipole polarizations at CEP = 0 (**c**) and CEP = 0.25π (**d**). The broad-band phase-flat SPM is corresponding to the ultrafast emission at time zero as a delta function, representing with the magenta arrow, whereas the dipole polarization of the Lorentz lineshape, i.e. $d(t)$ (complex-valued), is an amplitude-damped harmonic oscillation representing with the blue curve. At different CEPs, the azimuthal angle at the time zero is different. Only parallel components between SPM and air lasing result in the observed interference. In (**e**) we show the projections of $d(t)$ on the direction of SPM at CEP of 0 and 0.25π, respectively, where the relative phase shift between them is the so-called Fano phase Φ_{Fano}, which is labeled in (**e**) and strictly equal to $2\Phi_{CEP}$ in our case.

amplification occurring only at specific wavelengths. As highlighted in Fig. 4b, lasing intensities are prominently enhanced at wavelengths corresponding to J = 5, 6, 7, 8, 10, 12, 14, while those of J = 9, 11, 13, 15 remain approximately unamplified. The absence of amplification in odd-order rotational lasing lines at high J values demonstrates that population inversion is strongly influenced by the rotational population distributions of both the X and B states[14], which display a significant disparity between the two states. In the time domain, the pump and self-seed pulses overlap, preventing the macroscopic dipole polarization from fully building up. As a result, the amplification factor observed in our experiment is significantly weaker than in externally or delayed-seeded experiments[24].

In Fig. 4b, we also present the distribution of $\phi_0(\lambda)$. Distinct Lorentzian-shaped peaks are observed for each even-order transition line, accompanied by an arc-tangent-like π phase jump, in good agreement with our analysis in Fig. 3. For lower-order transitions, the presence of odd-order lines introduces irregular patterns in both the amplitude and phase profiles. In Fig. 4c, we disregard the energy dependence of the amplitudes of u and v, replacing them with their respective average values over the energy range. The main spectral features remain, indicating that the energy-dependent phase difference is the dominant factor shaping the observed spectra.

In conclusion, we have demonstrated an interesting N_2^+ air lasing experiment with CEP-stabilized few-cycle pulses. We observed that the lineshape of rotational lasing actions around 428 nm, corresponding to the transition from $B^2\Sigma_u^+(0)$ to $X^2\Sigma_g^+(1)$ in N_2^+ cations, are continually controlled between a symmetric Lorentz profile and an asymmetric Fano type. The CEP-dependent control of the lasing lineshape is explained and reproduced through the coherent superposition of the coherence established by the IR pulse and the SPM seed pulse. In this framework, the CEP is directly linked to the Fano phase factor in the time domain. Further data analysis demonstrates that the lasing emission lines are amplified at both even- and odd-order rotational transitions in the low-J regime, whereas in the high-J regime only even-order emission lines are prominently amplified. Our study highlights that electronic population inversion is not the sole determinant of air lasing intensity; molecular rotational dynamics also plays a crucial role.

Methods

Air lasing characteristics

To further verify that the observed forward-emission light is indeed air lasing rather than air fluorescence, we first measured the beam profile after the emission propagated over a distance of 5 meters in air, as shown in Supplementary Information Fig. 1a, b. Air fluorescence typically exhibits a large divergence angle, whereas air lasing is characterized by a much smaller divergence. In our measurements, the beam profile revealed a bright central spot enclosed by a donut-shaped ring. The outer donut-shaped pattern corresponds to the diffracted pump beam, shaped by the plasma filament, while the inner bright spot clearly indicates the forward-propagating air lasing beam.

https://doi.org/10.1038/s41467-025-65585-3

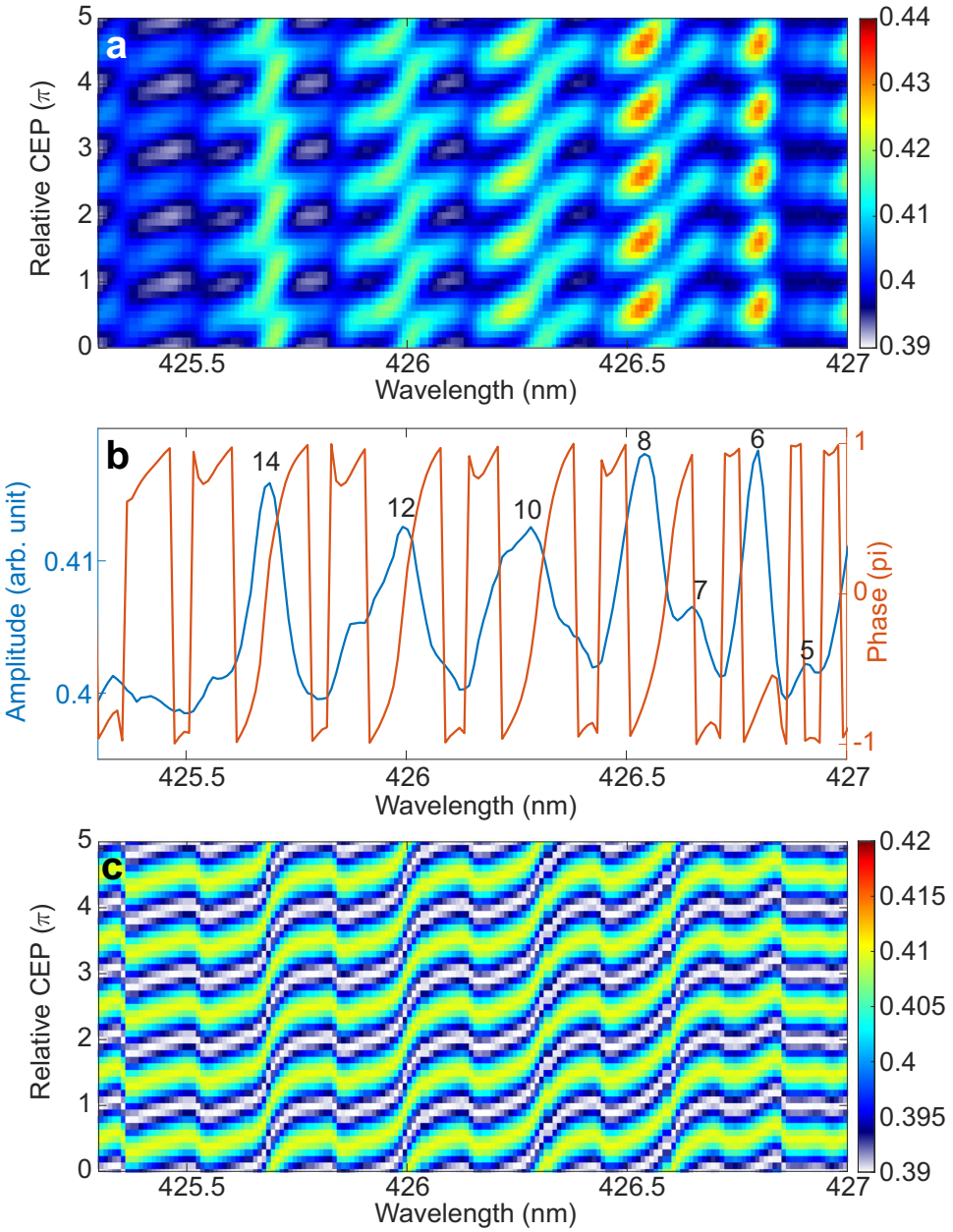

Fig. 4 | Amplification of rotational FID emission lines. a Fitting result of experimental data. At each wavelength, we fitted the experimental lineout by $a(\lambda) + b(\lambda)\cos[2\Phi_{CEP} - \phi_0(\lambda)]$ with the three free parameters: $a(\lambda)$, $b(\lambda)$ and $\phi_0(\lambda)$. **b** The fitting parameters of $a(\lambda)$ (blue curve) and ϕ_0 (orange curve). Note that $b(\lambda)$ is approximately 100 times smaller than $a(\lambda)$ and thus is not shown here. **c** The interference pattern by $\bar{a} + \bar{b}\cos[2\Phi_{CEP} - \phi_0(\lambda)]$.

The divergence angle of the air lasing emission is estimated to be less than 10 mrad. Additionally, we have checked the polarization state of the forward-emission air lasing and the side-emission air fluorescence. We use a lens to collect the emissions and then rotate the fast axis of a broadband UV polarizer (Thorlabs) before sending it into a common broadband spectrometer. The measured air lasing and fluorescence spectra as a function of the polarizer angle are shown in Supplementary Information Fig. 1d–e, respectively. The results confirm that the air lasing emission shares the same linear polarization as the SPM and THG signals, in contrast the air fluorescence is unpolarized.

Gas pressure dependence

We measured gas-pressure-dependence of the air lasing spectra from pure N_2. The CEP-resolved spectra at eight pressures (0.75, 10, 100, 200, 300, 400, 500, 600, 700 Torr) are shown in Supplementary Information Fig. 2. At low pressures (a, b, c), no clear CEP dependence was observed. However, as the pressure increased, the self-phase modulation (SPM) component was generated and thus the CEP dependence of the air lasing lines became apparent, as a clear evidence of the interference between air lasing and SPM. We also observed that the relative intensity between the 391 nm and 428 nm lasing lines varies with gas pressure. At low pressures (0.75–100 Torr), the 391 nm line dominates. At intermediate pressures (100–500 Torr), the 428 nm line becomes stronger. These trends are consistent with previous studies using 30-fs Ti:sapphire pulses. However, we further observed that at pressures above 600 Torr, the 391 nm line again becomes dominant. This reversal is attributed to the seeding effect of third-harmonic generation (THG). In contrast, previous Ti:sapphire-based studies did not report this second reversal, as the THG of 800 nm light does not coincide with the energy gap between the X and B states of N_2^+.

Data availability

The experimental data generated in this study have been deposited in the Zenodo database with the link: https://doi.org/10.5281/zenodo.17210855, see ref. 42.

Code availability

The code generated and/or analyzed during this study are available from the corresponding authors upon request.

References

1. Fano, U. Effects of configuration interaction on intensities and phase shifts. *Phys. Rev.* **124**, 1866 (1961).
2. Rost, J. M., Schulz, K., Domke, M. & Kaindl, G. Resonance parameters of photo doubly excited helium. *J. Phys. B Mol. Opt. Phys.* **30**, 4663 (1997).
3. Wickenhauser, M., Burgdörfer, J., Krausz, F. & Drescher, M. Time resolved Fano resonances. *Phys. Rev. Lett.* **94**, 023002 (2005).
4. Ott, C. et al. Lorentz meets Fano in spectral line shapes: a universal phase and its laser control. *Science* **340**, 716–720 (2013).
5. Ott, C. et al. Strong-field extreme-ultraviolet dressing of atomic double excitation. *Phys. Rev. Lett.* **123**, 163201 (2019).
6. Polynkin, P. & Cheng, Y. *Air Lasing*, vol. 206 (Springer, 2018).
7. Yao, J. et al. High-brightness switchable multiwavelength remote laser in air. *Phys. Rev. A* **84**, 051802 (2011).
8. Tong, X. M., Zhao, Z. X. & Lin, C. D. Theory of molecular tunneling ionization. *Phys. Rev. A* **66**, 033402 (2002).
9. Xu, H., Lötstedt, E., Iwasaki, A. & Yamanouchi, K. Sub-10-fs population inversion in N_2^+ in air lasing through multiple state coupling. *Nat. Commun.* **6**, 8347 (2015).
10. Yao, J. et al. Population redistribution among multiple electronic states of molecular nitrogen ions in strong laser fields. *Phys. Rev. Lett.* **116**, 143007 (2016).
11. Chen, Y. et al. Multiphoton resonance meets tunneling ionization: high-efficient photoexcitation in strong-field-dressed ions. *Phys. Rev. Lett.* **133**, 113201 (2024).
12. Yuen, C. & Lin, C. Probing vibronic coherence in charge migration in molecules using strong-field sequential double ionization. *Phys. Rev. A* **109**, L011101 (2024).
13. Yuen, C. & Lin, C. Density-matrix approach for sequential dissociative double ionization of molecules. *Phys. Rev. A* **106**, 023120 (2022).
14. Azarm, A., Corkum, P. & Polynkin, P. Optical gain in rotationally excited nitrogen molecular ions. *Phys. Rev. A* **96**, 051401 (2017).
15. Richter, M. et al. Rotational quantum beat lasing without inversion. *Optica* **7**, 586–592 (2020).
16. Kartashov, D. et al. Transient inversion in rotationally aligned nitrogen ions in a femtosecond filament. In *High Intensity Lasers and High Field Phenomena*, HTh4B–5 (Optica Publishing Group, 2014).
17. Zhang, H. et al. Rotational coherence encoded in an "air-laser" spectrum of nitrogen molecular ions in an intense laser field. *Phys. Rev. X* **3**, 041009 (2013).
18. Zeng, B. et al. Real-time observation of dynamics in rotational molecular wave packets by use of air-laser spectroscopy. *Phys. Rev. A* **89**, 042508 (2014).
19. Xu, H., Lötstedt, E., Ando, T., Iwasaki, A. & Yamanouchi, K. Alignment-dependent population inversion in N_2^+ in intense few-cycle laser fields. *Phys. Rev. A* **96**, 041401 (2017).
20. Liu, Z. et al. Near-resonant Raman amplification in the rotational quantum wave packets of nitrogen molecular ions generated by strong field ionization. *Phys. Rev. Lett.* **120**, 083205 (2018).
21. Arissian, L., Kamer, B., Rastegari, A., Villeneuve, D. & Diels, J.-C. Transient gain from N_2^+ in light filaments. *Phys. Rev. A* **98**, 053438 (2018).
22. Britton, M. et al. Short-and long-term gain dynamics in N_2^+ air lasing. *Phys. Rev. A* **100**, 013406 (2019).
23. Gao, J. et al. Controlling the polarization of nitrogen ion lasing. *J. Phys. Chem. Lett.* **15**, 3805–3811 (2024).
24. Xu, B. et al. Free-space N_2^+ lasers generated in strong laser fields: the role of molecular vibration. *Opt. Express* **26**, 13331–13339 (2018).
25. Wang, S. et al. Strong-field-induced N_2^+ lasing by phase control of free induction decay. *Phys. Rev. A* **108**, 033113 (2023).
26. Zhang, X. et al. Multiple-photon resonance enabled quantum interference in emission spectroscopy of N_2^+. *Ultrafast Sci.* **4**, 0051 (2024).
27. Ando, T. et al. Rotational, vibrational, and electronic modulations in N_2^+ lasing at 391 nm: evidence of coherent N_2^+ coupling. *Phys. Rev. Lett.* **123**, 203201 (2019).
28. Zhang, Q. et al. Sub-cycle coherent control of ionic dynamics via transient ionization injection. *Commun. Phys.* **3**, 50 (2020).
29. Yuen, C. & Lin, C. Theory of strong-field sequential double ionization of polyatomic molecules. *Phys. Rev. A* **109**, 033108 (2024).
30. Tsai, M.-S. et al. Nonlinear compression toward high-energy single-cycle pulses by cascaded focus and compression. *Sci. Adv.* **8**, eabo1945 (2022).
31. Han, M., Chen, M.-C., Tsai, M.-S. & Liang, H. Hearing carrier-envelope offset frequency and phase in air with a microphone. *Optica* **12**, 459–464 (2025).
32. Liang, H. et al. Waveform-dependent air fluorescence from neutral and ionic nitrogen molecules. *Sci. Adv.* **11**, eadu9200 (2025).
33. Cerullo, G., Baltuška, A., Mücke, O. D. & Vozzi, C. Few-optical-cycle light pulses with passive carrier-envelope phase stabilization. *Laser Photonics Rev.* **5**, 323–351 (2011).
34. Jones, D. J. et al. Carrier-envelope phase control of femtosecond mode-locked lasers and direct optical frequency synthesis. *Science* **288**, 635–639 (2000).
35. Apolonski, A. et al. Controlling the phase evolution of few-cycle light pulses. *Phys. Rev. Lett.* **85**, 740 (2000).
36. Kakehata, M. et al. Single-shot measurement of carrier-envelope phase changes by spectral interferometry. *Opt. Lett.* **26**, 1436–1438 (2001).
37. Baltuska, A. et al. Phase-controlled amplification of few-cycle laser pulses. *IEEE J. Sel. Top. Quantum Electron.* **9**, 972–989 (2003).
38. Fuji, T. et al. Monolithic carrier-envelope phase-stabilization scheme. *Opt. Lett.* **30**, 332–334 (2005).
39. Lei, H. et al. Ultraviolet supercontinuum generation driven by ionic coherence in a strong laser field. *Nat. Commun.* **13**, 4080 (2022).
40. Yuen, C.-H. & Lin, C.-D. Coherence from multiorbital tunneling ionization of molecules. *Phys. Rev. A* **108**, 023123 (2023).
41. Han, M. et al. Interference control of Fano resonances and dynamical imaging of an electron wave packet. *Ultrafast Sci.* **5**, 0091 (2025).
42. Han, M. Dataset for "controlling rotational air lasing lineshape by carrier-envelope offset phase". *Zenodo* https://doi.org/10.5281/zenodo.17210855 (2025).

Acknowledgements

We thank C. Aikens, S. Chainey and J. Millette for their technical support, and H. Lam for assistance with laboratory photography. Work at Kansas state university was supported by the Chemical Sciences, Geosciences and Biosciences Division, Office of Basic Energy Sciences, Office of Science, US Department of Energy, grant no. DE-FG02-86ER13491. M.-C.C. acknowledges the support from the National Science and Technology Council, Taiwan, grant no. 113-2112-M-007-042-MY3.

Author contributions

J.G., H.L. and M.Han conceived the study. J.G. and M.Han performed the experiments with the support of M.Hasan. C.H.Y. performed the simulations of the CEP dependence in the phase of FID. H.L. performed the

fitting. M.Han, H.L., M.-C.C., M.-S.T., C.-D.L., K.U. and H.J.W. analyzed and interpreted the data. M.Han and H.L. wrote the paper with the input from all authors.

Competing interests
The authors declare no competing interests.

Additional information
Supplementary information The online version contains supplementary material available at https://doi.org/10.1038/s41467-025-65585-3.

Correspondence and requests for materials should be addressed to Hao Liang or Meng Han.

Peer review information *Nature Communications* thanks Penji Ding, Yi Liu, and the other, anonymous, reviewer for their contribution to the peer review of this work. A peer review file is available.